Imperial College London

CCAP Centre for the Clinical Application of Particles

Space-charge lens for capture of a laser-driven ion beam

Titus-Stefan Dascalu

June 2020

CCAP-TN-ACCL-04

Contents

Section 1

Introduction

From the initial proposition of R. Wilson [1] in 1946 regarding the use of accelerated protons for radiotherapy, ion beams have proven to be an effective tool for cancer treatment. The key advantage of protons over X-rays is the precision with which the radiation dose can be delivered to the target tissue. In the context of a rising world population and an increase in the complexity of the disease, there is a urgent need for novel techniques to be developed in order to treat patients on a large scale and with the high precision necessary for a better quality of life. By February 2020, around 220,000 patients [2] have been treated with particle radiotherapy at 102 therapy facilities in operation worldwide. Approximately 80% of these patients were treated with proton beams, while for the others, light-ion beams were used - Fig. 1.1. Ions were clinically proven to have advantages for treatment such as higher damage to the target tissue and less energy deposition in the healthy tissue.

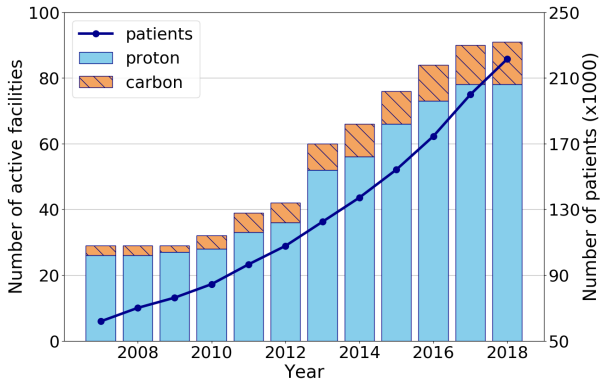

Figure 1.1: Statistics of patients treated in particle therapy facilities worldwide - data adapted from [2].

The main challenge in providing this treatment to a larger fraction of the population is to reduce the cost, size and the complexity of operation of the treatment facilities. The key element of such a facility is the accelerator. Most often, it dictates the specific requirements of the beam delivery system as well as the performance of the treatment facility. Further development is required to ensure that the treatment plan for patients will be determined by the clinical need and will not be limited by the accelerator technology.

Laser-driven ion beams have been proposed as an alternative to conventional accelerator facilities for radiotherapy applications as they can provide relatively higher dose rates and can produce light ions in addition to protons. Furthermore, laser and optical components are typically smaller and lighter compared with beam line magnets. The most attention has been devoted to TNSA (Target Normal Sheath Acceleration) [3]: a high intensity laser pulse is incident on a foil doped with hydrogen atoms. The energy absorption in the target creates a plasma and electrons are pushed out of the foil. The charge separation induces a strong electrostatic field which accelerates the protons out of the rear surface of the target.

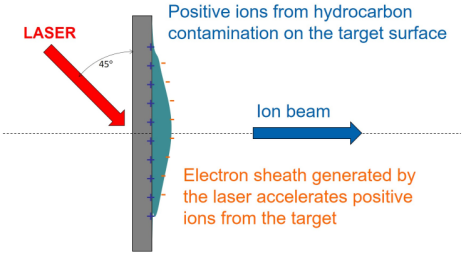

Figure 1.2: Schematic diagram illustrating the Target Normal Sheath Acceleration process (fig. obtained from [4]).

A large number of experiments have demonstrated the generation of multi-MeV proton and ion beams since the first report of laser acceleration of protons [5] in 2000 for several laser and target parameters. The energy spectra of the ion beams are broadband, typically with an exponential profile, up to a high energy cut-off [6]. The highest reported TNSA energies around 60 MeV were obtained using peta-watts lasers.

Motivation

The ion beams obtained by TNSA are superior to those of conventional RF beams in two main aspects: very low transverse emittance and high number of particles per shot. However, the beam has high divergence, high energy spread and low particle occupancy towards the high-energy end of the spectrum. These properties are listed in Table 1.1. Therefore, the design of an ion therapy facility based on TNSA has to solve the inherent challenges of capturing and focusing the ions obtained at the target to form a beam.

When compared to conventional proton and ion sources, laser pulses can accelerate ions to much higher energies. Conventional sources produce low energy particles (tens of keV/u). In such a beam, the electrostatic repulsion limits the total charge that can be captured and accelerated. Laser-driven ions are generated at higher energies (10 MeV or more) where the effect of space-charge forces becomes negligible. Consequently, the beam-current is only limited by the capacity of the capture system. The high particle flux produced at the target and the short duration of the particle bunch comparable to the laser pulse duration result in ultra-high instantaneous dose rates.

A space-charge lens is the optimal device to capture and focus the ion beam generated from the laser target, with the potential to fulfil the needs of an *in vitro* as well as of an *in vivo* facility. Its compact size, relative lower cost and ease of operation also make the lens suitable as a beamline component in future delivery systems for treatment facilities [7].

Furthermore, the laser-driven ion beams are a promising alternative in the view of new studies that support radiotherapy (RT) with ultra-high dose rates [8] (FLASH-RT). When compared to conventional radiotherapy, FLASH-RT was shown to reproducibly spare normal tissue for the same total amount of treatment dose [9]. Previous experiments using laser-driven proton beams [10] have reported on-cell instantaneous dose rates of the order of 10^9 Gy/s. By contrast, the beneficial different survival rate between tumour and normal tissue after FLASH irradiation was observed for dose rates well within the capabilities of laser-driven sources.

LhARA

The 'Laser-hybrid Accelerator for Radiobiological Applications', LhARA, is envisioned as a novel facility dedicated to the study of radiobiology [12]. The aim is to allow scientific contributions both as systematic studies of hadron interaction with living cells as well as technological research into laser-hybrid accelerators. The laser-hybrid approach can provide multiple ion species delivered at ultra-high dose rates with flexible temporal and spatial configurations.

A commercially available laser is planned to drive the production of a high flux of protons and light ions from a thin foil at a repetition rate of 10 Hz. The divergent beam is captured and focused by a sequence of two space-charge lenses. Downstream, three other lenses are used for matching and energy selection. A rapid post-acceleration would preserve the time and spatial structure of the beam dictated by the laser-driven source.

LhARA is planned to be developed in two stages. In Stage 1, a proton beam with energy between 10 MeV and 15 MeV will be delivered to an *in vitro* end station (see Fig. 1.3). In Stage 2, the beam will be accelerated by a fixed-field alternating-gradient accelerator (FFA) allowing both *in vitro* and *in vivo* experiments. In addition to proton beams with energy up to 127 MeV, ion beams will be available at energies of up to 33 MeV per nucleon. The beam energy at LhARA has been designed to allow *in vitro* experiments and *in vivo* studies on small mammals.

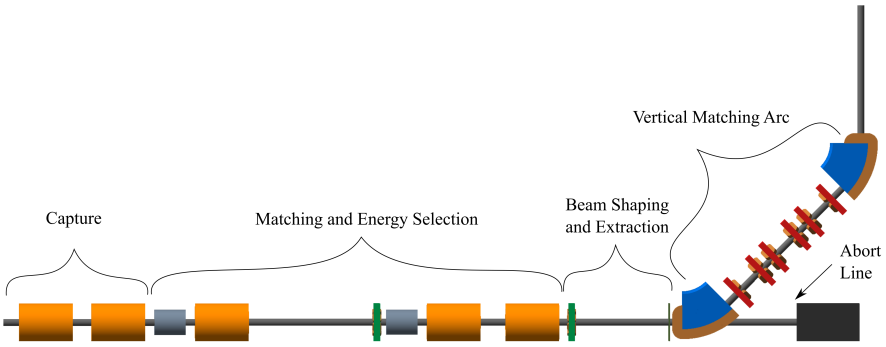

Figure 1.3: Beam line elements for LhARA Stage 1 visualised in BDSIM [11], showing the five main sections. The beam is produced at the target placed before the capture section and propagates from left to right and upwards trough the vertical arc. The Gabor lenses (orange cylinders) are the main component of the capture and energy selection systems. Two RF cavities are shown in grey and two octupole magnets in green. The vertical arc directs the beam into the low-energy *in-vitro* end station and is composed of two dipoles and six quadrupoles. A beam shaping collimator is placed before the arc (figure obtained from [12]).

Table 1.1: Properties of beams accelerated via TNSA (Target Normal Sheath Acceleration)

Characteristic	**Value**
ultra-low transverse emittance	> 0.004 mm-mrad
ultra-short bunch duration	≤ 1 ns
high brightness	$10^{11} - 10^{13}$ protons/shot
low number of protons at the high-energy end	$\sim 10^{6} - 10^{7}$ particles/MeV
large divergence	up to 10s of degrees, energy dependent
high energy spread	up to 100%$\Delta E/E$

Section 2

Basic principles of space-charge lenses

The concept of electrostatic focusing was first proposed in 1947 as the basis of the Gabor lens [13] – a confined electron plasma which theoretically can provide a linear axially symmetric space-charge force on the ion beam. While separate prototypes were built and investigated at several major particle physics laboratories around the world [14; 15; 16], the success for focussing low energy ion beams was overcome by the difficulty in balancing the operational electric and magnetic fields.

The leading advantage of the plasma lens is that the focal length is proportional to the kinetic energies of the ions within the beam. By comparison, the focal length of a solenoid is proportional to the square of the momentum and that of a quadrupole is proportional to the momentum [17]. Thus, at the clinically relevant energies, the space-charge lens is expected to provide better performance with a reduced magnetic field. Furthermore, a reduced focal length leads to a reduction in the footprint of the facility and thus in the total cost. The alternative optical systems such as solenoids and quadrupoles would have to operate at the technical limit which would drive the cost up.

A correspondence relation can be derived between the magnetic field B_{GL} of a Gabor lens and the magnetic field B_{sol} of a solenoid which have the same focusing strength for a beam of ions with charge Ze, mass m_{ion} and Lorentz factor γ_0 [18]:

$$B_{GL} = B_{sol}\sqrt{Z\frac{m_e}{m_{ion}}\frac{1}{\gamma_0}} \tag{2.1}$$

For instance, a Gabor lens would require a magnetic field smaller by a factor of 61 compared to a solenoid to ensure the same focusing strength for a carbon beam of energy 33 MeV/u.

Furthermore, a confined electron cloud could simultaneously reduce the emittance growth caused by external field errors and the influence of the beam self-charge, preserving the low emittance created in the laser-target interaction. These attractive features come at the cost of relatively high voltage operation and possible vulnerability to plasma instabilities.

Therefore, it is important that LhARA demonstrates the capability of space-charge lenses to capture and focus a laser-driven ion beam. A prototype of the lens [19] has been built at Imperial and tested using a 1 MeV proton beam at the Surrey Ion Beam Centre. Following these tests, the prototype is being upgraded as part of an extensive R&D process planned in two phases.

Phase 1 focuses on verifying the high vacuum operation and characterising the focusing properties under steady-state conditions. At the same time, numerical plasma modelling is used to study the collective instabilities and to optimise the electron cloud production. An online, non-invasive diagnostic technique is being developed in order to measure the electron density inside the lens.

Phase 2 will use the results from numerical simulations of stability as input for a lens designed and built for pulsed operation. The plasma will be generated by an electron emitter incorporated inside the lens in accordance to the numerical studies of electron trajectories necessary to form the space-charge cloud.

Overall, the R&D work is aimed at proving the stable operation of a space-charge lens at the design parameters of LhARA and developing suitable instrumentation.

Other applications

The main short-term application of a space-charge lens could be the production of nuclides which would benefit from an increased production rate and the possibility to vary the projectile ion and its energy. Commercially available laser systems can produce protons with energies exceeding 25 MeV. This is sufficient for producing the widely used medical isotope Tc^{99} from Mo^{99} [20] or for the production of F^{18}, C^{11}, N^{13}, O^{15} used in positron emission tomography (PET) [21]. A lattice combining space-charge lenses and RF cavities may offer a factor of 10 improvement in energy resolution compared to aperture collimation alone [7]. Such a lattice would be suited to investigate the variation of the production yield with the beam energy.

A second application may be possible in fast-ignition of inertial fusion targets by laser-driven ion beams. Numerical simulations suggested that quasimonoenergetic proton and carbon beams have better coupling with the compressed targets and significantly lower ignition rates when compared to Maxwellian energy distributions [22]. Ion energy spreads as high as 40% may be acceptable. Furthermore, for quasimonoenergetic ions, the ion source can be placed further away from the fuel capsule, simplifying the target design. However, monoenergetic beams have low laser-to-ion conversion efficiencies, often an order of magnitude lower than beams with Maxwellian energy distributions [23]. A system based on space-charge lenses may ensure the required focusing of the ions onto the target as well as a quasimonoenergetic energy profile while benefiting from the higher efficiency of production mechanisms with a broad ion energy spectrum. The main challenge would be to design the capture and focusing optics such that the ion beam requirements at the target correspond to optimal ignition of the fuel capsule [24].

Longitudinal confinement

A system of electrodes such as that presented in Fig. 2.1 is used to create a potential well which traps the electrons longitudinally. A stable dynamic equilibrium was previously obtained with a variety of electrode and magnetic field configurations [25]. For our design, the configuration is similar to a Penning-Malmberg trap [26; 27] since it offers excellent access to the plasma column, see Fig. 2.1. A further useful feature is the simple harmonic motion of the trapped particles in the combined electric and magnetic fields. Measuring the characteristic oscillation frequencies allows the investigation of some properties of the plasma.

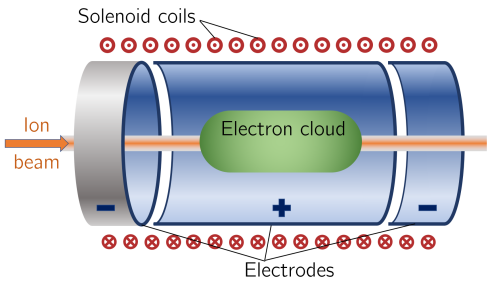

Figure 2.1: The main components of a Penning-Malmberg trap proposed for use in the Gabor lenses. The longitudinal magnetic field is produced by the solenoid coils indicated by the red circles. A central cylindrical anode and two cylindrical negative cathodes produce the confining electrostatic potential. The electron cloud in green is expected to occupy the interior volume of the anode.

Assuming a cold, homogeneous electron plasma column of density n_e extending to a radius R_A, the space-charge potential can be obtained as

$$\Phi_r(r) = -\int_0^{R_A} E_r(r)dr = \frac{n_e e R_A^2}{4\epsilon_0} \qquad (2.2)$$

Electrons start to escape from the longitudinal potential barrier when the space-charge potential is equal to the potential difference between the anode and the cathode $\Phi_r = V_A$. Thus, the maximum longitudinal confinement is reached for an electron density

$$n_{e,l,max} = \frac{4\epsilon_0 V_A}{e R_A^2} \qquad (2.3)$$

Here, we have assumed that the anode and cathode have the same internal radius R_A, that the cathode is grounded and that the anode has a

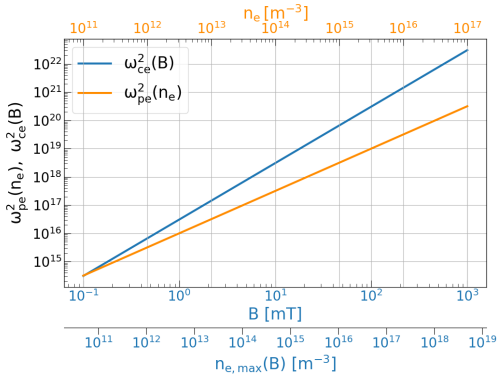

Figure 2.2: Electron plasma frequency ω_{pe} and electron cyclotron frequency ω_{ce} plotted as a function of magnetic field B (blue) and electron density n_e (orange) respectively. The second horizontal axis under the figure shows the maximum electron density which can be confined by the corresponding magnetic field B.

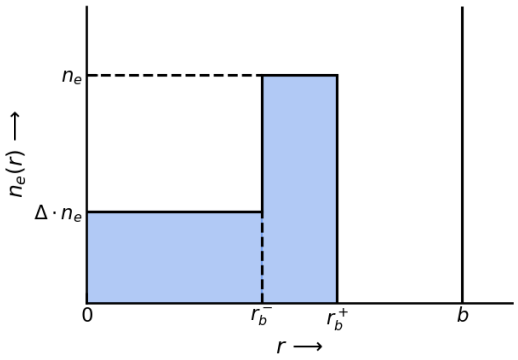

Figure 2.3: Radial electron density $n_e(r)$ for a step-function profile with inverted population and a degree of hollowness Δ inside a conducting cylinder of radius b.

potential V_A. For a cathode and anode with different radii, loss channels may form between the two electrodes and the radius of the plasma column may differ from the radius of the anode [28].

Radial confinement

An axial uniform magnetic field causes the electrons to exhibit spiral trajectories parallel to the axis of the lens, thus confining them in the radial direction. The initial proposal by Gabor [13] included a ring-shaped thermionic cathode placed in a magnetic field cusp where $B = 0$ for the electrons to be emitted with zero canonical angular momentum. This initial state allows the formation of a Brillouin-flow (or rigid rotor) equilibrium [29].

The force balance equation between the Lorentz, electrostatic and centrifugal forces leads to two possible mean angular velocities [30]

$$\omega_E^{\pm} = \frac{\omega_{ce}}{2}\left[1 \pm \left(1 - \frac{2\omega_{pe}^2}{\omega_{ce}^2}\right)^{\frac{1}{2}}\right] \tag{2.4}$$

where ω_{pe} is the electron plasma frequency and ω_{ce} is the electron cyclotron frequency. ω_E^+ corresponds to a gyration of electrons around the central axis, whereas ω_E^- is characteristic to an $E \times B$ rotation of the plasma column. The Brillouin flow is achieved at the high electron density limit where

$$2\omega_{pe}^2 = \omega_{ce}^2 \tag{2.5}$$

The maximum radial electron density can be extracted from the above condition as

$$n_{e,r,max} = \frac{\epsilon_0}{2m_e} B^2 \tag{2.6}$$

An additional factor $(1 - f)$ can be included to account for the interaction of electrons with the residual gas ions which form a neutralising background with a fractional neutralisation $f = \text{const}$. A correspondence between the axial magnetic field B and the maximum confined electron density $n_{e,r,max}$ can be seen on the two horizontal axes at the bottom of Fig. 2.2.

To compare the numerical simulations or experimental results with the theory and to measure the trapping efficiency, the filling factors κ_l and κ_r are introduced, where

$$\kappa_l = \frac{n_{e,l}}{n_{e,l,max}} \qquad \kappa_r = \frac{n_{e,r}}{n_{e,r,max}} \tag{2.7}$$

While previous experiments and numerical simulations have shown average filling factors up to $60 - 70\%$ [28; 31], space-charge becomes advantageous for beam focusing at $\kappa \gtrsim 25\%$ [16].

Assuming the same equilibrium density in the longitudinal and radial directions $n_{e,r,max} = n_{e,l,max}$, one can define a theoretical work function for the lens which relates the axial magnetic field B and the applied potential V_A [29]

$$V_A = \frac{eR_A^2}{8m_e} B^2 \tag{2.8}$$

It is important that this work function be validated through both numerical simulations and experiments in parallel with developing instrumentation to measure the confined electron density. For LhARA to deliver beams with different energies and ion species, it is required that the focal length of each space-charge lens be accurately controlled. Thus, a good understanding of the electron density and plasma stability along with the work function (2.8) is necessary.

Diocotron instability

One of the most common instabilities in a low density non-neutral electron plasma is the diocotron instability [32; 33]. It was first observed in low-current annular electron beams [34], but it is also typical for electron plasma columns confined radially by a uniform axial magnetic field B. Its driving mechanism is an azimuthal shear in the angular $\boldsymbol{E} \times \boldsymbol{B}$ rotation velocity, $\omega_E(r) = -E_r(r)/rB$, of the plasma. Here, $E_r(r)$ is the equilibrium radial electric field. The instability is important in strong magnetic fields for which $\omega_{pe}^2/\omega_{ce}^2 \ll 1$. Fig. 2.2 shows a comparison between ω_{pe} and ω_{ce} for different values of the electron plasma density n_e and external magnetic field B. While at the Brillouin flow limit, which gives the radial confinement condition, the ratio $\omega_{pe}^2/\omega_{ce}^2$ is 1/2, stronger magnetic fields may be required in an experimental setup, thus lowering this ratio well below 0.5.

Previous numerical simulations and electron density measurements suggested that the diocotron instability appears in several versions of the Gabor lens when the parameters of the lens are tuned away from its work function [35; 36]. Numerical simulations show that the diocotron instability is linked to annular electron profiles. This can be explained as the interaction between two waves propagating along the inner and outer surfaces of the ring. An additional factor believed to promote the instability is the residual gas pressure as electrons loose energy in the collisions with residual gas molecules [37].

The stability of the diocotron mode is strongly dependent on the radial electron density profile. A uniform density distribution corresponds to rigid rotation of the plasma column which is always stable. Any non-uniformity causes a shear in adjacent azimuthal layers of plasma which leads to instability. Thus, a necessary condition for instability is that $\partial n_e/\partial r$ changes sign over the interval $0 \leq r \leq b$ where b is the radius of the conducting cylinder within which the plasma is confined [30]. Such an inverted population is described by the general simplified density profile shown in Fig. 2.3 and corresponding to the step-function

$$n_e(r) = \begin{cases} \Delta \cdot n_e = \text{const.}, & 0 \leq r < r_b^-, \\ n_e = \text{const.}, & r_b^- < r < r_b^+, \\ 0, & r_b^+ < r \leq b. \end{cases} \tag{2.9}$$

Here, the parameter Δ varies from $\Delta = 1$ (uniform density distribution) to $\Delta = 0$ (annular density profile), the plasma column becoming strongly unstable towards lower values of Δ. The proximity of the outer conducting wall at radius b also influences the stability.

Such a density profile offers a first-order approximation to some of the electron density distributions observed later in numerical simulations (see Fig. 3.9 and Fig. 3.11). Furthermore, there is theoretical reason to expect a hollow electron cloud when the external magnetic field is larger than the value required to confine a specific electron density [38]. At stronger magnetic fields, the gyration radius of the electrons becomes smaller and the electron column is compressed. Thus, the local electron density exceeds the confinement limit given by the anode potential and electrons escape from the central region.

A linear stability analysis of the diocotron modes was derived in [39] for both the electron density profile drawn in Fig. 2.3 and for a more general continuously-varying profile. Starting from a self-consistent Poisson equation, an eigenvalue equation is derived for low-frequency electrostatic flute perturbations (perturbations extended along magnetic field lines). For the step-function density profile in eq. (2.9) and the appropriate boundary conditions the following dispersion relation is obtained [39]

$$\left(\frac{\omega}{\omega_D}\right)^2 - 2\hat{b}\left(\frac{\omega}{\omega_D}\right)^2 + \hat{c} = 0 \tag{2.10}$$

where the geometrical factors $\hat{b}$ and $\hat{c}$ are defined by

$$2\hat{b} = l[1+\Delta-(1-\Delta)(r_b^-/r_b^+)^2]-\{[1-(r_b^+/b)^{2l}] - (1-\Delta)[1-(r_b^-/b)^{2l}]\} \quad (2.11)$$

$$\hat{c} = l^2[1-(1-\Delta)(r_b^-/r_b^+)^2]\Delta-\{l[1-(r_b^+/b)^{2l}]\Delta - l[1-(r_b^-/b)^{2l}](1-\Delta)[1-(1-\Delta)(r_b^-/r_b^+)^2] + (1-\Delta)[1-(r_b^-/r_b^+)^{2l}][1-(r_b^+/b)^{2l}]\} \quad (2.12)$$

and $\omega_D \equiv \frac{\omega_{pe}^2}{2\omega_{ce}}$ represents the diocotron frequency and l the instability mode number.

The solution to the dispersion relation is given by

$$\omega = \omega_D \left[\hat{b} \pm (\hat{b}^2 - \hat{c})^{1/2}\right] \quad (2.13)$$

from which the necessary and sufficient condition for instability is

$$\hat{c} > \hat{b}^2 \quad (2.14)$$

Whenever the instability condition is met, the growth rate is $\mathrm{Im}(\omega) = (\hat{c} - \hat{b}^2)^{1/2}\omega_D$.

In the special case $\Delta = 0$, Fig. 2.4 shows the instability regions of the diocotron modes $l = 2, 3, 4$ for an annular electron density profile. For a fixed value of r_b^-/b, a sufficiently large value of r_b^+/b leads to stability. Thus, the proximity of the outer conducting wall has a stabilising influence on the diocotron modes [30].

A different behaviour is seen for the more general case $\Delta \neq 0$. Fig. 2.5 shows the stability-instability contours for the first three unstable diocotron modes l . The instability condition (2.14) is met inside the closed contours. As the electron density profile becomes less hollow, the parameter space corresponding to instability is reduced and it shift towards values of r_b^+/b closer to 1. As the mode number l increases, the instability regions move towards the 45° line.

Consequently, in practice, the lens has to be filled as homogeneously as possible in order to operate in a regime away from the diocotron instability. The homogeneity can be controlled to a certain degree by ensuring that the electrons are emitted from a cathode with a wide range of transverse canonical momenta. Separately, the axial magnetic field may lead to the formation of a hollow plasma column if not properly matched to the local electron density.

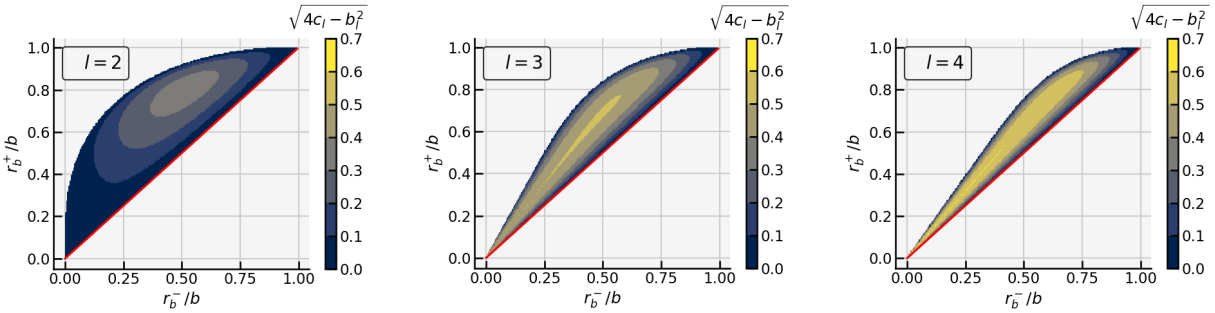

Figure 2.4: Instability regions of the diocotron mode l for an annular electron density profile ($\Delta = 0$) extending from radius r_b^- to r_b^+ inside a cylindrical conductor of radius b. A higher geometrical coefficient $\sqrt{4c_l - b_l^2}$ corresponds to a higher instability growth rate ($b_l \equiv 2\hat{b}$, $c_l \equiv \hat{c}$ for $\Delta = 0$). An unstable solution exists only in the region above the red line where $r_b^+ > r_b^-$. The system is always stable for the fundamental mode $l = 1$.

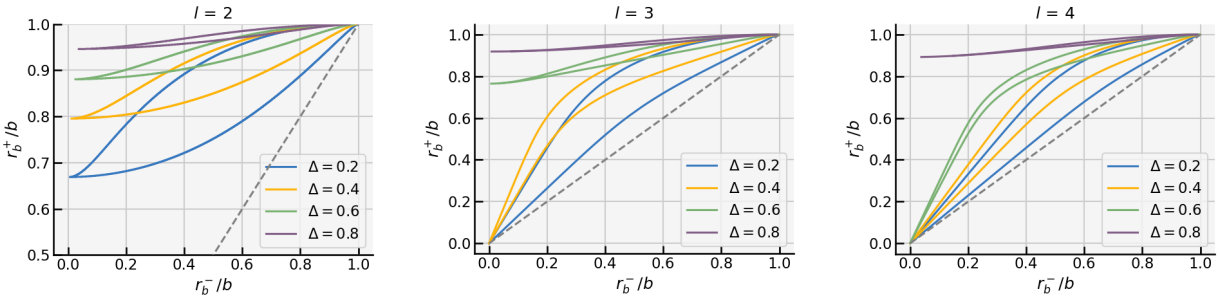

Figure 2.5: Stability-instability contour plots of the diocotron mode l given by $\hat{b}^2 = \hat{c}$ as obtained from equations (2.11) and (2.12) for the step density profile described in Fig. 2.3. Four filling factors $\Delta = 0.2, 0.4, 0.6, 0.8$ are shown for each mode. The condition for instability is met in the regions inside the closed contours. A physical solution exists only above the dashed line where $r_b^+ > r_b^-$.

Section 3

Initial studies

3.1 Energy selection

In both treatment delivery and radio-biological studies, there are specific maximum uncertainties for the beam parameters which can be allowed such that the treatment is safe or the delivered dose is known with high accuracy. For pencil beam scanning the maximum tolerable energy spread is 1-2%, while for radio-biology applications the energy spread can rise to the level of ±2% [40].

To minimise the required laser intensity and, thus, the cost of the laser system, the nominal beam energy of 15 MeV is found towards the end of the broad energy spectrum of the particles produced in the laser-target interaction. In this region centred around 15 MeV, the energy spectrum is quasi-flat over a large interval of more than ±5%. Filtering such an energy spread and collecting the laser-produced beam with large divergence requires a unique focusing system and beam optics.

The beamline for LhARA stage 1 is designed to be compact by using three space charge lenses and one collimator for energy selection. The advantage of a plasma lens is that the focal length is proportional to the kinetic energy of the particles entering the lens. Thus, if an aperture is positioned at the focus of the particles of reference energy, off-energy particles are removed from the beam. This scheme is highly flexible allowing for a fast change of the reference energy by adjusting the voltage and magnetic field of the three lenses. Under the thin lens approximation and at low energies, the required change in voltage is linear with the change in energy, while the magnetic field scales with the square root of the beam energy [18].

In previous models of the stage 1 beamline for LhARA, the space charge lenses were modelled as solenoids with an equivalent focusing strength. However, a more appropriate model of the lenses was needed which allows for an energy dependent focal length. To verify the energy selection scheme and the beam optics of the stage 1 beamline, the previous optics were computed again by modelling each plasma lens as both a thick element transfer matrix and as an ideal electron cloud.

Since the solenoidal magnetic field required to confine the electron cloud is of the order of 1-50 mT, it can be neglected in the beam dynamics calculations. Therefore, in the presence of only an electrostatic field, the particle dynamics in a straight geometry is described by the following Hamiltonian [17]

$$H = \frac{\delta}{\beta_0} - \sqrt{\left(\delta + \frac{1}{\beta_0} - \frac{q\phi}{cP_0}\right) - p_x^2 - p_y^2 - \frac{1}{\beta_0^2\gamma_0^2}} \tag{3.1}$$

where $\delta = \frac{E}{cP_0} - \frac{1}{\beta_0}$ is the energy deviation, ϕ is the electrostatic potential, $P_0 = \beta_0\gamma_0 mc$ is the reference momentum of a particle with mass m, energy E, charge q and normalised canonical momentum $p_{x,y} = \frac{\beta_{x,y}\gamma mc}{P_0}$.

After applying the appropriate confinement condition [18] on the space-charge cloud, the maximum electron density can be obtained from the external magnetic field B_{GL} according to eq. (2.6). Given the electron density $n_{e,max}$ one readily obtains the electrostatic potential ϕ of a uniform cylindrical electron distribution and the associated electric field

$$E_r = -\frac{en_e}{2\epsilon_0}r \tag{3.2}$$

The Hamiltonian (3.1) can be liniarised under the paraxial approximation ($p_x, p_y \ll 1; x, y \ll 1\,\mathrm{m}$) and under the condition of low voltage ($q\phi \ll cP_0$) to obtain

$$H_2 = \frac{p_x^2}{2} + \frac{p_y^2}{2} + \frac{\delta^2}{2\beta_0^2\gamma_0^2} + \frac{k}{2}(x^2+y^2) + O(3) \quad (3.3)$$

For the full relativistic case and an ideal lens filling factor (maximum electron density), the focusing strength k is given by

$$\frac{k}{2} = \frac{1}{2}\frac{qe}{4\gamma_0 m_e m_{ion}\beta_0^2 c^2} B_{GL}^2 \quad (3.4)$$

where q and m_{ion} represent the charge and mass of the ion species traversing the lens.

Consequently, the focal length of a space-charge lens can be derived from the focusing strength k and

$$\frac{1}{f} = \sqrt{k}\sin(\sqrt{k}L) \quad (3.5)$$

where L is the effective length of the lens.

Thus, this model of the lens allows the implementation of this device in two different ways in a tracking code:

(a) as a linear transfer matrix for a thick element in the $(x, p_x, y, p_y, z, \delta)$ phase-space

$$R_{GL} = \begin{pmatrix} \cos(\omega L) & \frac{\sin(\omega L)}{\omega} & 0 & 0 & 0 & 0 \\ -\omega\sin(\omega L) & \cos(\omega L) & 0 & 0 & 0 & 0 \\ 0 & 0 & \cos(\omega L) & \frac{\sin(\omega L)}{\omega} & 0 & 0 \\ 0 & 0 & -\omega\sin(\omega L) & \cos(\omega L) & 0 & 0 \\ 0 & 0 & 0 & 0 & 1 & \frac{L}{\beta_0^2\gamma_0^2} \\ 0 & 0 & 0 & 0 & 0 & 1 \end{pmatrix}$$

where $\omega = \sqrt{k}$

(b) as an ideal electric field map generated according to equation (3.2).

While method (a) is a useful verification of the beam dynamics, method (b) will be preferred later as it allows for particles with different energies to focus at different positions along the beam-line. Tracking each particle through the electrostatic field allows a study of the energy selection scheme. A more realistic implementation is planned in the near future by extracting the electric field map from a numerical simulation of the plasma using a PIC code.

The matrix method was implemented into two tracking codes (MADX [41] and BDSIM [11]) for which the beam optics were benchmarked against each other. MADX is a code for optics design in an accelerator beam-line. BDSIM is a Monte-Carlo simulation tool for studying beam transport, loss and interaction with matter in a particle accelerator. The electrostatic field map was loaded into the BDSIM simulation and the beam optics was compared with the alternative implementations. Figure 3.1 shows very good agreement between the beta functions obtained with solenoids and with the two more realistic implementations of the plasma lenses. Further agreement is seen in all the other beam optics functions.

Having obtained the beta functions β_x, β_y along the beamline, the position of the energy collimator is chosen to coincide with the focal point of the beam after the first three plasma lenses. Thus, the rectangular collimating aperture is placed before the first octupole magnet at the minimum of both β_x and β_y.

To verify the energy selection scheme, a primary beam of 10^5 protons and a flat kinetic energy distribution of $15\,MeV \pm 5\%$ was tracked through the full beamline using BDSIM. Fig. 3.2 shows the effect of the collimating aperture on the kinetic energy distribution of the beam for three different diameters of the collimator. An arbitrary length of 1 cm was chosen for the collimator. After the aperture, the energy pro-

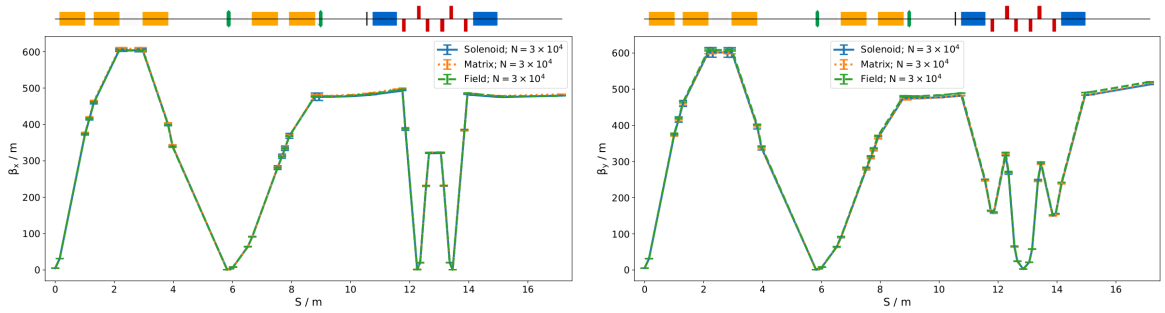

Figure 3.1: Horizontal (left) and vertical (right) betatron function β_x, and β_y respectively, in LhARA Stage 1 simulated with BDSIM using N particles. The beamline elements are shown above the figure. The Gabor lenses are shown as orange cylinders, while the quadrupole, dipole and octupole magnets are shown in blue, red and green respectively. Each set of points corresponds to a different implementation of the lens as a solenoid, transfer matrix or field map.

file is centred at the reference energy of 15 MeV and it is represented by a Gaussian-like peak with heavy tails. A smaller aperture reduces the width of the central peak, while the tails remain present in all the three cases. For an aperture smaller than about 0.5 mm, particles are lost even at the reference energy.

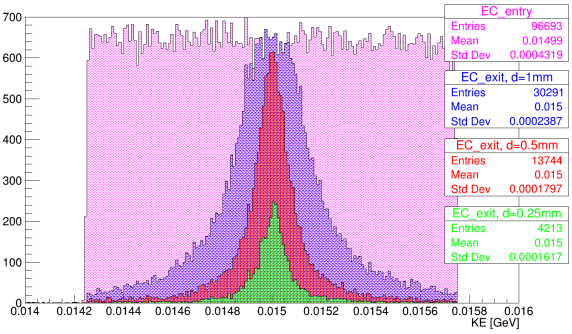

Figure 3.2: Kinetic energy distribution at the entry and exit faces of the energy collimator as simulated in BDSIM. The primary beam has a flat energy profile of 15 $MeV \pm 5\%$ shown in magenta. The collimated energy profile is shown for three different apertures: 1mm (blue), 0.5mm (red), 0.25mm (green). Full agreement is obtained within the numerical errors as expected.

Based on the result seen in Fig. 3.2, the collimation scheme was extended by adding two other apertures as shown in Fig. 3.3. A second circular collimator is placed before the vertical arc to absorb the particles with high transverse momentum and shape the beam. A third elliptical collimator is positioned in the middle of the arc at large dispersion to cut the high-momentum tails. Figure 3.4 confirms that a final energy spread can be obtained within the maximum accepted value of $\pm 2\%$ with a relatively highly populated peak and no energy tails. Further optimisation of the collimator sizes may be possible to ensure that fewer particles are lost from the central peak. The loss of particles with the correct energies at the second collimator is associated with the effect of the first octupole magnet which causes some particles of reference energy to populate the halo of the beam.

Following the confirmation obtained above, further cases were simulated. A beam distribution obtained from the simulation of the laser-target interaction was tracked through the same beamline. Due to the small number of particles in the initial distribution, no conclusions could be taken on the efficiency of the collimating scheme on this particular beam. Additionally, the target energy spread was also confirmed for a beam of carbon ions with the same rigidity as a 15 MeV proton beam.

3.2 Plasma lens simulations

One important step in the design stage of the space-charge lens is to verify the stability of the non-neutral plasma for the required electron density ($10^{14} - 10^{16}\,\mathrm{m}^{-3}$) and cathode potentials ($1 - 50\,kV$). To model the plasma instabilities, we chose a 3D particle-in-cell (PIC) code called VSim [42] because of its wide capabilities and previous experience within the groups that are members of the LhARA consortium. Access to it was obtained on the HPC cluster

Figure 3.3: The beamline elements for LhARA Stage 1. The Gabor lenses are shown as orange cylinders, while the quadrupole, dipole and octupole magnets are shown in blue, red and green respectively. The black vertical bars mark the position of collimators for: 1-energy selection, 2-beam shaping, 3-momentum cleaning. The collimators 1 and 3 have been added to the previous beam line design.

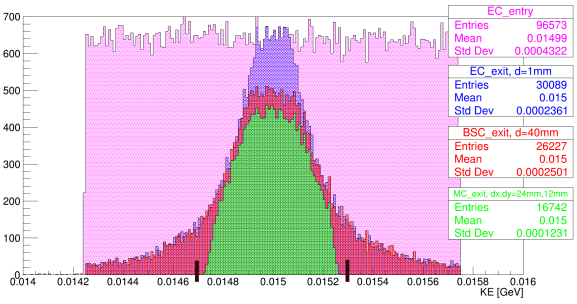

Figure 3.4: Kinetic energy distribution at the exit faces of each collimator in the beamline as simulated in BDSIM. The effect of the energy collimator is shown in blue, beam shaping in red and momentum cleaning in green. The black bars on the horizontal axis mark the maximum accepted energy spread of ±2%.

SCARF [43] provided by STFC Scientific Computing Department. The code is designed to run computationally intensive plasma simulations in parallel in the presence of electrostatic fields and complex geometries. While there are built-in post-processing tools, these were not available at the time of this report, so that separate analysis scripts were written and used to produce the results presented in this section.

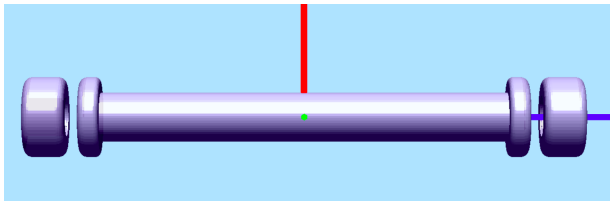

Figure 3.5: Geometry of the plasma lens visualised in VSim: the anode in the middle and two cathodes at the sides. The vacuum vessel which encloses the entire system is not shown.

The geometry of the lens was built using the VSim Visual Composer, maintaining all the features present in the current design and providing easily accessible parameters to change all the important specifications. Figure 3.5 shows the main elements of the lens which were previously described in diagram 2.1. All the electrodes are isolated from the vacuum vessel. There are two options to operate with either a grounded anode or a grounded cathode. The curved edges ensures that the electric field for the maximum cathode voltage of 100 kV is well below the conventional break-down limits of suitably prepared surfaces. The design parameters are summarised in Table 3.1.

While the initial studies were done with an external spatially uniform magnetic field, there is a plan to introduce solenoid coils in the model for a more realistic magnetic field. The configuration of the coils is still in the design phase in order to optimise the distribution of the field lines. As the conservation of angular momentum forces the electrons to orbit around the magnetic field lines, the configuration of the coils may affect the filling of the lens. This is planned along with introducing an electron emitter such as a thermionic cathode in the available space between one cathode and the anode to obtain a uniform filling of the lens.

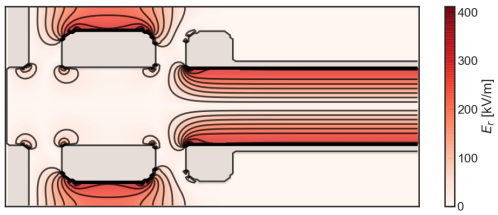

Figure 3.6: Radial electric field and equipotential lines for a cathode potential of 6 kV and uniform electron density $n_e = 1 \times 10^{15}\, m^{-3}$ inside the volume of the anode. From left to right: entrance wall of the vacuum vessel, cathode, anode (longitudinal cross-section).

After the geometry was completed. a first electrostatic simulation of the lens was run without the space-charge inside the anode. The aim

Table 3.1: Specifications for the current design of the space-charge lens

Parameters	**Value**
Lens length	1.157 m
Lens effective length (anode length)	0.857 m
Cathode length	0.08 m
Anode cathode gap	0.025 m
Anode internal radius	0.0365 m
Vacuum vessel internal radius	0.1 m
Anode-cathode voltage design value	65 kV
Solenoidal magnetic field design value	50 mT
Electron number density	$\approx 5 \times 10^{15}\,\mathrm{m}^{-3}$

was to verify that the setup corresponds to the design and benchmark the break-down electric field against results obtained with a different simulation tool. Furthermore, this initial set of simulations offered a measure of the computing time required for a specific user-defined resolution. A higher limit was achieved for a grid size of $100 \times 100 \times 500$ cells (x, y, z directions) after which some tasks in the simulation exceed the available memory per core. Figure 3.6 shows a typical electric field distribution which in this case corresponds to the confining potential for an electron density of $n_e = 1 \times 10^{15}\,m^{-3}$. The maximum radial electric field appears on the curved external surface of the cathode. The current maximum electric field is 7.7 MV/m obtained at the maximum design cathode voltage of 100 kV which is well below conventional break-down limits. Further optimisation is possible by increasing the radius of curvature at the corners.

Lens filling

VSim uses macroparticles to simulate an ensemble of physical particles. The macroparticles can be either emitted from a user-defined surface or they can be introduced in the simulation volume before the initial time step. A macroparticle is initialised by specifying its phase-space coordinates $(x, y, z, \gamma v_x, \gamma v_y, \gamma v_z)$.

We have chosen to start the simulation with a homogeneous distribution of electrons inside the volume of the anode. Similar initial conditions were used in previous observations of the diocotron instability in space-charge lenses [44]. The initial electron density, n_e, is a simulation parameter and it is set to match the nominal electron density of the lens. The solenoidal magnetic field and the cathode voltage are derived starting from n_e according to the radial and longitudinal confinement conditions respectively (eqs. 2.3 and 2.6).

For each macroparticle, the velocity components are independently sampled from a Gaussian distribution which corresponds to thermal equilibrium in the absence of the electrostatic potential. The velocity distribution is fully determined by the non-neutral plasma temperature T_e. Based on previous simulation results and measurements [35], we chose $T_e = 100\,\mathrm{eV}$.

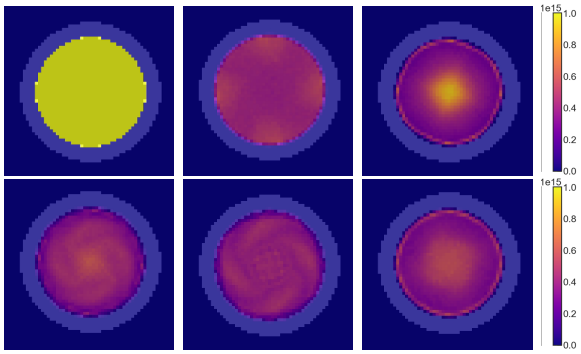

Figure 3.7: Electron density distributions at different time steps during numerical simulation for an initial $n_e = 1 \times 10^{15}\,m^{-3}$ (transverse cross-sections along the anode). The characteristic ring-like and spiral distributions appear periodically during the full simulation.

Electron cloud dynamics

Several initial simulations were done in VSim to investigate the features of the confined electron

plasma for specific cathode voltages and external magnetic fields as well as to characterise any instability that may appear.

The first results shown in Fig. 3.7 were obtained by running a simulation of the space-charge lens with an initial electron density $n_e = 1 \times 10^{15}\, m^{-3}$ for 300 steps (≈ 50 ns). The cathode voltage (6 kV) and the external magnetic field (14 mT) were set according to the theoretical confinement conditions (2.3) and (2.6) for a nominal electron density equal to the initial n_e. In both radial and axial directions, the electron cloud fully fills the internal volume of the anode. No longitudinal instability or plasma break-up has been seen. In the transverse plane, Fig. 3.7 shows an accumulation of electrons in the centre and edges of the column at specific time steps. In between, the plasma exhibits a spiral shape with four arms which periodically appear in the centre and fade away towards the edges with a period of about 2 ns.

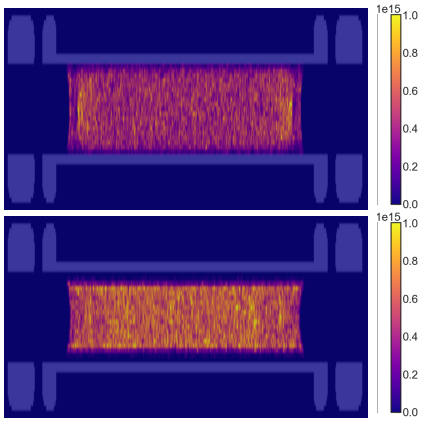

Figure 3.8: Longitudinal cross-section of the plasma lens showing the electron density $[m^{-3}]$ at two different time steps. The effective length of the plasma column is shorter than the length of the anode due to the mismatch in cathode potential and nominal electron density. A periodic radial contraction of the plasma column is seen during the full simulation, while the length remains constant.

A second simulation was run with the same initial and nominal electron density $n_e = 1 \times 10^{15}\, m^{-3}$. The strength of the magnetic field was matched to the electron density, while the cathode potential was set to its maximum design value of 100 kV. Fig. 3.8 shows the main result: increasing the cathode potential over the value required to confine the electron density n_e leads to particles being lost at the edges of the plasma column, thus reducing the effective length of the space-charge cloud below the length of the anode. Furthermore, the plasma column contracts and dilates radially with a constant period of about 7 ns. Fig. 3.8 shows the maximum and minimum radial extent of the plasma column. Looking at the total particle number in the simulation, two sources of particle loss were identified. During a short time period at the beginning of the simulation, particles are lost from the left and right edge of the plasma column due to the mismatch in the cathode potential. Afterwards, particles are only absorbed at the internal surface of the anode when the plasma column reaches its maximum radial amplitude. Thus, the absorbed current at the anode is seen to have an identical period to the radial oscillation of the electron cloud. Consequently, increasing the axial magnetic field strength may suppress the radial oscillation and some of the particle loss.

Accordingly, the next simulation was run with a cathode voltage matched to the electron density n_e, but with a magnetic field strength increased from 13 mT to 100 mT. Also, the total duration of the simulation was increased to 1000 time steps (≈ 180 ns) to allow for possible instabilities with lower growth rates to develop. Previous numerical simulations show the formation of a hollow plasma column after about 40 μs [37]. A first observation was that the average electron density does not decrease below the initial value n_e in the initial time steps. This suggests that the electrons are more strongly confined in the transverse direction and do not reach the surface of the anode. As time evolves, the average electron density remains at the nominal value starting to develop a depression in the centre of the column to about 0.8 of the nominal density (see Fig.3.9). Similar hollow profiles were also observed when measuring the light emitted longitudinally by the plasma after times of order 10 ms [37]. Current effort is done to improve the speed of the simulation to allow an observation of the plasma dynamics for times up to milliseconds.

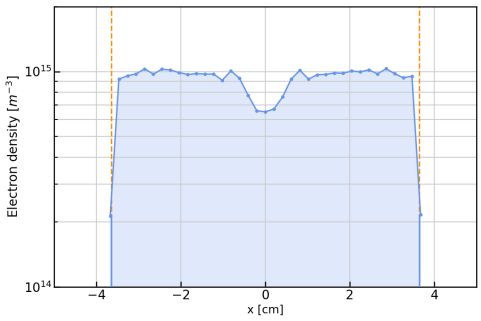

Figure 3.9: Averaged radial electron density profile after approximately 200 ns. The initial density was set to $1 \times 10^{15}\,\mathrm{m}^{-3}$ and magnetic field to 100 mT. A depression starts to form near the axis of the lens. The vertical dashed lines mark the edges of the anode.

Radial electric field

The focusing quality of the space-charge lens is highly dependent on the homogeneity of the electron density distribution. Any deviation of the radial focusing electric field from linearity causes spherical aberrations. These can be caused either by the radius of the electron cloud being smaller than the radius of the beam or by a non-homogeneous charge distribution of the plasma. Beam transport measurements under several electron density profiles showed strong spherical aberrations which lead to "S"-like shapes of the beam phase space distribution [38]. This should be avoided under steady state operation of the lens by maintaining the homogeneity of the electron cloud.

To study the linearity of the radial electric field in our setup, we extracted an averaged electron density and electric field from the numerical simulations. Two frames separated by about 5 ns are shown in fig. 3.11. As a first feature, after the initial time step, the average electron density oscillates around an equilibrium value which is approximately 50% of the initial charge density. One possible cause for the oscillation is believed to be the difference between the actual equilibrium state of the confined plasma column and the initial thermal equilibrium assumed in the absence of any electrostatic field. The two types of density distributions shown in Fig. 3.11 appear periodically during multiple time steps. The second density profile which is peaked towards the edges of the plasma column may lead to the diocotron instability known to be driven by negative radial gradients in the space-charge density.

A second important feature seen in fig. 3.11 is the linearity of the radial electric field up to about two thirds or 2.5 cm of the anode internal radius. With the current beamline design for LhARA Stage 1, the 2σ beam envelope reaches a maximum value of 2.8 cm which may suggest that a larger anode diameter is required for the lens to keep the beam passing through the homogeneous region of the plasma.

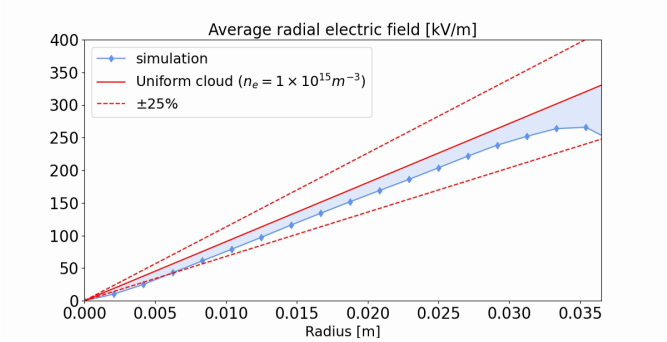

Figure 3.10: Averaged radial electric field as a function of radius for the electron density profile shown in Fig. 3.9. The data points obtained from simulation are shown in blue. The solid red line represents the theoretical expectation value for a uniform electron distribution.

If increasing the magnetic field above the value required for confinement will prove not to cause a hollow profile and instabilities, this could be a method to prevent the oscillation of the electric field. Fig. 3.10 shows the averaged radial electric field for the density profile in Fig 3.9. The numerical data is much closer to the theoretical expected value and indicates a larger linear region. However, the focusing strength is seen to be different near the axis ($0\,\mathrm{m} \leq r \leq 0.01\,\mathrm{m}$) compared to the edge of the plasma column ($0.01\,\mathrm{m} \leq r \leq 0.03\,\mathrm{m}$).

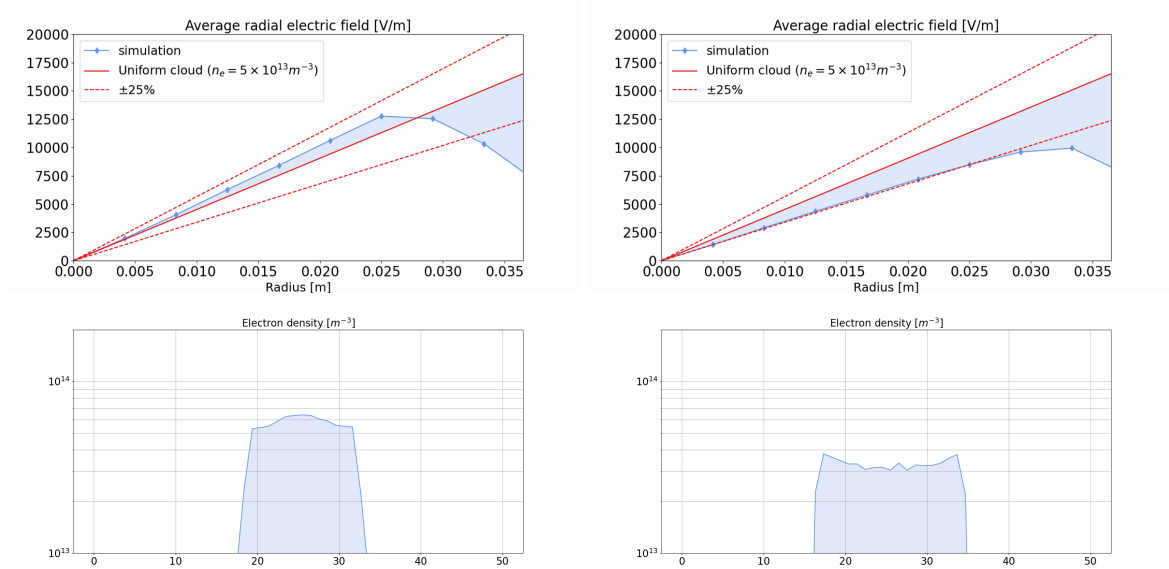

Figure 3.11: Radial electric field and corresponding electron density averaged over two transverse directions and longitudinally over the length of the electron cloud for an initial charge density $n_e = 1 \times 10^{14}\, m^{-3}$. Two time steps are extracted form the evolution of the confined plasma to show an oscillation of the magnitude of the radial electric field and average electron density. Top: the red line depicts an ideal linear electric field about which the numerical result in blue oscillates. Bottom: The radial gradient of the electron density changes sign during the simulation. The horizontal axis has arbitrary units.

Section 4

Future work

Future work is planned based on the R&D programme developed for the capture section of LhARA [45]. The main technical challenges and planned studies are presented below.

Lens operation

A first aim is to characterise the operation of the space-charge lens at the design parameters of LhARA. This will involve a determination of the working point of the lens in terms of the relation between applied voltage, magnetic field and electron density, its maximum achievable filling factors and confirmation of the focusing strength and quality.

As a pre-requisite, a verification is planned for the high-voltage electrode and vacuum systems which should ensure a reliable operation of the lens. Due to the poor vacuum conditions around the laser target, a differential pump port was designed to ensure different high-vacuum conditions in the region of the lens.

Instrumentation

As an accurate control of the focal length of each lens is critical for delivering a beam with the correct characteristics to the end stations, the electron density within the lens needs to be measured or monitored. We aim to measure the phase shift of an RF wave caused by the refractive index change. Numerical models have been constructed and an experimental verification is planned. Although this method is non-invasive and can be done online, it has some identified limitations. Alternatively, other techniques demonstrated in literature, such as energy spectrometry of the emitted ions [44], will be developed.

Additionally, the performance of the lens will be measured by studying the beam parameters at the input and output of the lens. As an initial test, an alpha source can be used to mimic the LhARA source at slightly lower energies. A sealed alpha source is proposed to be introduced in the vacuum camber of the lens, shaping the beam with appropriate collimating apertures. A thin fluorescent film placed at the exit of the lens will detect the beam position and profile after passing through the electron plasma.

Stability

A further important aim is to demonstrate the reliable operation of a space-charge lens in a regime free of the diocotron instability. This will be done in the following steps: understanding the conditions under which the instability occurs, reproducing some experimental results where the instability was recognised before, designing a lens which can operate outside of the unstable regime. Numerical modelling of the plasma dynamics has been started and will guide the next iterations of the design of the lens. A separate simulation is currently prepared to reproduce the effects observed with an ion beam for the previous prototype of the lens.

If the steady state operation proves to be unstable, a second generation space-charge lens could be designed and built for pulsed operation. An electron emitter introduced inside the lens allows the generation of the plasma. Consequently, the nominal electron density could be achieved and the beam could pass through the lens in a time interval shorter than the time taken by an instability to develop.

References

[1] R. R. Wilson, "Radiological use of fast protons," *Radiology*, vol. 47, no. 5, pp. 487–491, 1946. https://doi.org/10.1148/47.5.487. 1

[2] "Particle therapy co-operative group." https://www.ptcog.ch/index.php/patient-statistics. [Accessed: 18-February-2020]. 1

[3] S. C. Wilks *et al.*, "Energetic proton generation in ultra-intense laser–solid interactions," *Physics of Plasmas*, vol. 8, no. 2, pp. 542–549, 2001. 1

[4] A. Kurup *et al.*, "Simulation of a radiobiology facility for the centre for the clinical application of particles," *Physica Medica*, vol. 65, pp. 21 – 28, 2019. 1

[5] E. L. Clark *et al.*, "Measurements of energetic proton transport through magnetized plasma from intense laser interactions with solids," *Physical Review Letters*, vol. 84, no. 4, pp. 670–673, 2000. 2

[6] M. Borghesi, "Laser-driven ion acceleration: State of the art and emerging mechanisms," *Nucl. Instr. and Meth. in Phys. Res., Section A: Accelerators, Spectrometers, Detectors and Associated Equipment*, vol. 740, pp. 6–9, 2014. 2

[7] J. Pozimski, M. Aslaninejad, and P. A. Posocco, "Advanced Gabor Lens Lattice for Laser Driven Hadron Therapy and Other Applications," in *7th International Particle Accelerator Conference*, p. TUPMY023, 2016. 2, 5

[8] M.-C. Vozenin *et al.*, "The advantage of flash radiotherapy confirmed in mini-pig and cat-cancer patients," *Clinical Cancer Research*, vol. 25, no. 1, pp. 35–42, 2019. 2

[9] V. Favaudon *et al.*, "Ultrahigh dose-rate flash irradiation increases the differential response between normal and tumor tissue in mice," *Science Translational Medicine*, vol. 6, no. 245, pp. 245ra93–245ra93, 2014. 2

[10] D. Doria *et al.*, "Biological effectiveness on live cells of laser driven protons at dose rates exceeding 109 Gy/s," *AIP Advances*, vol. 2, no. 1, p. 011209, 2012. 2

[11] L. J. Nevay *et al.*, "Bdsim: An accelerator tracking code with particle-matter interactions," *Computer Physics Communications*, p. 107200, 2020. 3, 11

[12] G. Aymar *et al.*, "The Laser-hybrid Accelerator for Radiobiological Applications," *arXiv e-prints*, p. arXiv:2006.00493, May 2020. 2, 3

[13] D. GABOR, "A Space-Charge Lens for the Focusing of Ion Beams," *Nature*, vol. 160, no. 4055, pp. 89–90, 1947. 4, 6

[14] J. Palkovic *et al.*, "Measurements on a Gabor Lens for Neutralizing and Focusing a 30 Kev Proton Beam," *Proc. LINAC88*, pp. 179–181, 1988. 4

[15] A. Goncharov *et al.*, "Some characteristics of moderate energy metal ion beam focusing by a high current plasma lens," *Review of Scientific Instruments*, vol. 69, no. 2, pp. 1135–1137, 1998. 4

[16] J. Pozimski, R. Dölling, P. Gross, and H. Klein, "Investigation of Space Charge Compensated Transport by Use of a Gabor Plasma Lens," no. 1, pp. 80–82. 4, 6

[17] A. Wolski, *Beam dynamics in high energy particle accelerators*. London: Imperial College Press, 2014. 4, 10

[18] J. Pozimski and M. Aslaninejad, "Gabor lenses for capture and energy selection of laser driven ion beams in cancer treatment," *Laser and Particle Beams*, vol. 31, no. 4, p. 723–733, 2013. 4, 10

[19] P. A. Posocco, M. J. Merchant, J. Pozimski, and Y. Xia, "First test of the imperial college gabor (plasma) lens prototype at the surrey ion beam centre," 2016. 4

[20] T. Ruth, "Accelerating production of medical isotopes," *Nature*, vol. 457, no. 7229, pp. 536–537, 2009. 5

[21] E. Lefebvre *et al.*, "Numerical simulation of isotope production for positron emission tomography with laser-accelerated ions," *Journal of Applied Physics*, vol. 100, no. 11, p. 113308, 2006. 5

[22] J. J. Honrubia *et al.*, "Fast ignition of inertial fusion targets by laser-driven carbon beams," *Physics of Plasmas*, vol. 16, no. 10, p. 102701, 2009. 5

[23] J. Fuchs *et al.*, "Laser-driven proton scaling laws and new paths towards energy increase," *Nature Physics*, vol. 2, no. 1, pp. 48–54, 2006. 5

[24] J. J. Honrubia and M. Murakami, "Ion beam requirements for fast ignition of inertial fusion targets," *Physics of Plasmas*, vol. 22, no. 1, p. 012703, 2015. 5

[25] R. Mobley, G. Gammel, and A. Maschke, "Gabor lenses," *IEEE Transactions on Nuclear Science*, vol. 26, no. 3, 1979. 5

[26] J. S. deGrassie and J. H. Malmberg, "Waves and transport in the pure electron plasma," *The Physics of Fluids*, vol. 23, no. 1, pp. 63–81, 1980. 5

[27] J. H. Malmberg *et al.*, "Experiments with pure electron plasmas," *AIP Conference Proceedings*, vol. 175, no. 1, pp. 28–74, 1988. 5

[28] J. Pozimski and O. Meusel, "Space charge lenses for particle beams," *Review of Scientific Instruments*, vol. 76, no. 6, p. 063308, 2005. 6

[29] M. Reiser, "Comparison of gabor lens, gas focusing, and electrostatic quadrupole focusing for low-energy ion beams," in *Proc. of the 1989 IEEE Ptcl. Acc. Conf., . 'Accelerator Science and Technology*, pp. 1744–1747 vol.3, 1989. 6

[30] R. C. Davidson, *Physics of nonneutral plasmas*. Imperial College Press London, 2001. 6, 7, 8

[31] O. Meusel, *Fokussierung und Transport von Ionenstrahlen mit Raumladungslinsen*. PhD thesis, Johann Wolfgang Goethe-Universität, 2006. 6

[32] R. H. Levy, "Diocotron instability in a cylindrical geometry," *The Physics of Fluids*, vol. 8, no. 7, pp. 1288–1295, 1965. 7

[33] W. Knauer, "Diocotron instability in plasmas and gas discharges," *Journal of Applied Physics*, vol. 37, no. 2, pp. 602–611, 1966. 7

[34] R. L. Kyhl and H. F. Webster, "Breakup of hollow cylindrical electron beams," *IRE Transactions on Electron Devices*, vol. 3, no. 4, pp. 172–183, 1956. 7

[35] M. Droba *et al.*, "Studies on Electron Cloud Dynamics for an Optimized Space Charge Lens Design," *Conf. Proc. C*, vol. 110904, pp. 3495–3497, 2011. 7, 14

[36] M. Droba *et al.*, "High-Current Beam Transport Simulations Including Gabor Lenses in Varying Non-Neutral Plasma States," in *4th International Particle Accelerator Conference*, p. TUPWO008, 2013. 7

[37] K. Schulte *et al.*, "Electron cloud dynamics in a gabor space charge lens," *IPAC 2012 - International Particle Accelerator Conference 2012*, vol. 0, no. 1, pp. 1164–1166, 2012. 7, 15

[38] Schulte, Kathrin, *Studies on the Focusing Performance of a Gabor Lens Depending on Non-neutral Plasma Properties*. PhD thesis, Johann Wolfgang Goethe-University, Frankfurt am Main, 2013. 7, 16

[39] R. C. Davidson and G. M. Felice, "Influence of profile shape on the diocotron instability in a non-neutral plasma column," *Physics of Plasmas*, vol. 5, no. 10, pp. 3497–3511, 1998. 7

[40] S. Giordanengo and M. Donetti, "Dose Delivery Concept and Instrumentation," in *CAS - CERN Accelerator School: Accelerators for Medical Applications*, pp. 13–47, 2 2018. 10

[41] "Methodical Accelerator Design X." `http://madx.web.cern.ch/madx`. 11

[42] "Vsim for plasma," 2020. `https://www.txcorp.com/vsim`. 12

[43] "Scientific Computing Resources for Facilities," 2020. `https://www.scarf.rl.ac.uk/home`. 13

[44] O. Meusel, M. Droba, B. Glaeser, and K. Schulte, "Experimental studies of stable confined electron clouds using Gabor lenses," *Conf. Proc. C*, vol. 1206051, pp. 157–160, 2013. 14, 18

[45] G. Aymar *et al.*, "The Laser-hybrid Accelerator for Radiobiological Applications," Tech. Rep. CCAP-TN-01, Imperial College London, 04 2020. 18